Research Square

Preprints are preliminary reports that have not undergone peer review.
They should not be considered conclusive, used to inform clinical practice,
or referenced by the media as validated information.

Effect of β precipitate size on the short-term high temperature oxidation resistance in γ-β two phase alloy

Zhentao Wang
Graduate school of engineering, Hokkaido University
Suzue Yoneda
Hokkaido University
Ali Shaaban
Hokkaido University
Mitsutoshi Ueda
Hokkaido University
Shigenari Hayashi
hayashi@eng.hokudai.ac.jp
Hokkaido University

Research Article

Keywords: short-term high temperature oxidation, Ni-Cr-Al-Fe alloy, γ-β two phase alloy, precipitate size, Al2O3 formation

Posted Date: September 1st, 2026

DOI: https://doi.org/10.21203/rs.3.rs-10750548/v1

License: This work is licensed under a Creative Commons Attribution 4.0 International License.
Read Full License

Additional Declarations: No competing interests reported.

Abstract

The effect of β precipitate size on the short-term oxidation behavior of a γ-β two phase Ni-12Al-20Cr-15Fe-0.03Zr alloy at 1000°C was systematically investigated. The β precipitate size was found to significantly influence the initial oxidation behavior and the resulting oxide scale structure. The supersaturated single-γ sample formed a continuous and homogeneous duplex oxide scale consisting of an outer Cr_2O_3 layer and an inner Al_2O_3 layer. In contrast, samples with coarser β precipitates exhibited higher mass gain and a larger area fraction of a thick oxide scale consisting of Cr_2O_3 and internal Al_2O_3 precipitates. A continuous single θ-Al_2O_3 scale formed above the β precipitates, which was attributed to delayed transition to α-Al_2O_3 due to the limited formation of Cr_2O_3. In the regions surrounding β precipitates, a thin oxide scale similar to that formed on the supersaturated single-γ samples was observed. This was attributed to the combined supply of Cr from the γ matrix and Al supply from the rapidly dissolving β precipitates at the β/γ interfaces. These results demonstrate that β precipitate size is a critical microstructural parameter controlling local Al and Cr supply, and therefore governs the initial oxidation behavior and oxide scale structure of γ-β two phase Ni-based alloys.

1. Introduction

High temperature alloys are designed to exhibit superior machinal properties at elevated temperatures, for instance, in applications such as gas turbines, jet engines [1], and related fields [2, 3]. Most high-temperature structural materials are designed as multiphase alloys, in which mechanical performance is enhanced through precipitation strengthening. Thus, extensive research has investigated the effects of alloys microstructure on mechanical properties. However, alloy microstructure influences not only the mechanical properties but also high temperature oxidation behavior [4–6].

In our previous study, we investigated the effect of precipitate size on the high temperature oxidation behavior of a Ni-based alloy with a γ-γ’ two phase structure and found that γ’ precipitate size affects the initial oxidation process [7]. In particular, fine precipitates enhanced the Al supply to the surface during this initial stage of oxidation, owing to the faster decomposition of γ’-precipitates associated with a higher γ/γ’ interface density. In contrast, the precipitate size had little effect on the long-term oxidation kinetics. These findings suggest that precipitate size plays an important role in the establishment and growth of a protective Al_2O_3 scale during the period when a high Al flux is required. However, in γ-γ’ two phase alloys, the influence of precipitate size on oxidation behavior is limited, because the equilibrium difference in Al concentration between the γ and γ’ phases is small.

In β (NiAl) phase containing Ni-based alloys [8, 9], the β phase is expected to improve the mechanical properties of Ni-based high temperature alloys [10–13]. Owing to their high Al content, β precipitates can also act as an Al reservoir for the formation of a protective Al_2O_3 scale through dissolution during oxidation [14–16]. At the same time, precipitation of the β phase reduces the Al content in the γ-matrix, which may decrease the ability of the matrix to form a protective Al_2O_3 scale [17]. Therefore, β-γ two

phase alloys provide a suitable system for clarifying the effect of precipitate size on the high temperature oxidation behavior of Ni-based alloys.

In such alloys, the precipitate size is expected to strongly affect the competition between Al consumption in the γ-matrix and Al replenishment from β precipitates through dissociation and diffusion process [18]. This competition may lead to apparent difference in high temperature oxidation performance among alloys with different precipitate size. Because the effective Al supply from β precipitates depends on the γ/β interface density, where precipitate dissolution occurs [19], the size of β precipitates directly determines the interface density in this system. Thus, β precipitate size is expected to be a critical microstructural parameter governing high temperature oxidation behavior.

In this study, we focused on the spatially resolved formation of oxides above γ and β regions and on the detailed microstructure of oxide scale formed in the samples with different precipitate size. We investigated the effect of β precipitate size on the short-term high temperature oxidation resistance of a γ + β two-phase Ni-based model alloy containing Al (12 at. %), Cr (20 at. %), and Fe (15 at %). A small amount of Zr (0.03 at. %) was added to enhance the spallation resistance of the oxide scale.

2. Experimental procedure

A γ-β two-phase alloy with a nominal composition of Ni-12Al-20Cr-15Fe-0.03Zr (at. %) was used in this study. Zr was added to improve the adhesion of the oxide scale and suppress oxide scale spallation [20, 21]. Alloy ingots were prepared by argon arc melting using high-purity metals: Al (99.99%), Cr (99.99%), Ni (99.99%), Fe (99.99%) and Zr (99.99%). All ingots were homogenized at 1200°C for 24 h under vacuum. Samples with a supersaturated single-γ structure and with three different β precipitate sizes were prepared through different heat treatments. The ingots were solution-treated at 1250°C for 1 h in evacuated quartz tubes and then quenched into water to obtain the supersaturated single-γ samples. For the samples with different β precipitate sizes, the single-γ samples were cold rolled by 50%, annealed at 1000°C for 1, 100, or 500 h in evacuated quartz tubes, and finally air-cooled. The initial alloy microstructure was characterized using a field-emission scanning electron microscope (FE-SEM; JSM7200F) equipped with an energy-dispersive X-ray spectrometer (EDS). Prior to observation, the samples were ground with SiC abrasive papers up to 4000 grit, polished with 3 μm and 1 μm diamond suspensions and finished with 0.01 μm colloidal SiO_2. The grain sizes of samples were evaluated using optical microscopy after chemical etching in an acid solution of 16 ml HCl, 4 ml HNO_3, and 20 ml H_2O for 7–10 min.

Samples with a thickness of approximately 1.5 mm were cut from heat-treated ingots. The samples were ground using SiC abrasive papers up to 4000 grit and then polished with a 3 μm diamond suspension. Isothermal oxidation experiments were conducted at 1000°C in a vertical furnace with a sample elevation unit [22] for short-term oxidation tests for up to 60 min. The samples reached 1000°C within approximately 4 min in the vertical furnace.

After oxidation, the mass gain of each sample was measured using a microbalance with a sensitivity of 0.1 μg. The oxidation products were characterized using X-ray Diffractometer (XRD; Smart Lab), FE-SEM, electron probe micro analyzer (EPMA; JXA-8530F), and scanning transmission electron microscope (STEM; HD-2000) operated at 200 kV. A focused ion beam (FIB; FB-2100) was used to prepare the STEM samples. For STEM cross-sectional observations, a W-protective layer was deposited prior to FIB milling to prevent damage from Ga ion irradiation. Cross-sectional lamellae were prepared by lift-out and attached to a Cu grid. Microstructural observations were performed in bright-field (BF) mode, and chemical compositions were analyzed using EDS. For cross-sectional observations of oxide scales using FE-SEM and EPMA, the samples were mounted in a cold resin, sectioned, ground using SiC abrasive papers up to 4000 grit, and polished with 3 μm and 1μm diamond suspensions.

3. Results

3.1 Microstructures of samples

Figure 1 shows the microstructure of the supersaturated single-γ phase and the γ-β two-phase samples with different β precipitate sizes. In the supersaturated single-γ phase sample, a homogeneous γ matrix was observed. Because the shape of precipitates formed in the γ-β two-phase samples were not spherical, the β precipitate size was defined as the largest length of precipitates, and it was summarized in Fig. 1 (i-k). The precipitate sizes of the fine-sized (FS), medium-sized (MS), and coarse-sized (CS) samples were approximately 0.5–1.5 μm, 3–4 μm, and 5–9 μm, respectively. The volume fraction of β precipitates, quantified using ImageJ software, was approximately 17% in all two-phase samples. Figure 1 **(b, d, f, h)** shows the optical microscopy images of the samples after etching for 7–10 min in an acid solution of 4 ml HNO_3, 16 ml HCl, and 20 ml H_2O. Although the grain boundaries are not clearly visible in the optical micrographs shown in Fig. 1 **(d, f, h)**, the SEM images reveal grains with different contrast. The grain size of the CS sample was larger than those of the other samples; however, the grains were sufficiently larger than the β precipitates in all samples. Therefore, the influence of grain size is considered to be minor compared with that of β precipitate size.

Considering the irregular precipitates formed in the γ-β two-phase samples, an approximate calculation of interfacial surface density using simplified ideal sphere models was conducted. In a 10*10*2 μm^3 region, the precipitate size was 0.5–1.5 μm in the FS samples, 3–4 μm in the MS samples, and 5–9 μm in the CS samples. The precipitates volume fraction in both samples is similar, f = 0.17. Using the sphere-precipitate approximation, the phase boundary density (area of phase boundary per unit volume) is calculated to be approximately 0.170–0.510 μm^{-1} in the FS samples, 0.064–0.085 μm^{-1} in the MS samples, and 0.283–0.510 μm^{-1} in the CS samples.

EPMA analysis revealed that the compositions of the γ matrix and β phase in the CS sample were 53.9Ni-8.7Al-21.2Cr-16.1Fe and 58.2Ni-28.2Al-6.3Cr-7.3Fe (at. %), respectively, as summarized in Table 1. The composition of the γ and β phases in the MS sample were similar to those in the CS sample. Although the β phase in the FS sample was too small for quantitative analysis by EPMA, the composition

of the γ and β phases in the FS sample were also similar to those in the CS and MS samples. Assumption that the effect of Fe on the oxidation behavior is negligible, the oxide map of the Ni-Al-Cr system at 1000 ℃ [23–25], shown in Fig. 2, indicates that the composition of the γ matrix lies within the internal oxidation region, whereas that of the β precipitate lies within the Al_2O_3 formation region.

Table 1
Chemical compositions of the γ and β phases measured by EPMA in at. %

phase	Ni	Al	Cr	Fe
γ	**53.9**	**8.7**	**21.2**	**16.1**
β	58.2	28.2	6.3	7.3

3.2 oxidation kinetics

Figure 3 shows the oxidation kinetics of samples oxidized at 1000 ℃ in air for up to 60 min. Each data point represents the average mass gain obtained from two to three samples. The mass gain remained relatively low for all samples but increased with increasing β precipitate size. The difference in oxidation kinetics was most pronounced during the initial oxidation stage, approximately with the first 10 min, indicating that β precipitate size primarily affects the early stage of oxidation. Thereafter, the oxidation rates became low and nearly identical among the samples, suggesting that a protective Al_2O_3 scale had formed on the surface.

3.3 Oxidation for up to 10 min

Figure 4 shows the initial alloy microstructures and the surface morphologies of the oxide scales formed on the samples at the same positions before and after oxidation for 10 min. The supersaturated single-γ sample formed a homogeneous oxide scale, whereas all samples containing β precipitates formed inhomogeneous oxide scales. The inhomogeneity of the oxide scale depended on the initial microstructure of the substrate. In the CS sample, a thick oxide scale formed above the γ matrix region, whereas a relatively thin oxide scale formed above the β precipitates. In addition, a very thin oxide scale formed above the β/γ interfaces. A similar distribution of oxide scales was observed in the MS sample; however, the oxide scale formed above the β precipitates tended to be very thin, presumably due to the higher density of β/γ interfacial regions. The oxide scale formed on the FS sample showed the same tendency as that on the MS sample, but this tendency became more pronounced. In the FS sample, the area covered by the thick oxide scale area was very small and most of the surface was covered by a very thin oxide scale formed above the interfacial regions and a relatively thin oxide scale formed above β precipitates. The area fraction of the thick oxide scale formed above the γ matrix region depended on the β precipitate size. Although the area fraction of β precipitates was nearly constant among the FS, MS, and CS samples, the area fraction of the thick oxide scale was highest in the CS sample, approximately 81.7%, compared with approximately 74.3% in the MS sample. The area fraction of the thick oxide scale

formed on the FS sample was difficult to quantify using Image-J software because each region was difficult to distinguish; however, it was clearly much smaller than those in the MS and CS samples. This difference in the area where a thick oxide scale formed resulted in the difference in mass gain shown in Fig. 3.

Figure 5 shows the XRD profiles of the samples before and after oxidation for 10 min. After oxidation for 10 min, θ-Al_2O_3 was not detected for the supersaturated single γ sample; only α-Al_2O_3 peaks were detected among the Al_2O_3 phases, together with Cr_2O_3 peaks. In contrast, both θ-Al_2O_3 and α-Al_2O_3 were detected for the samples containing β precipitates, irrespective of the β precipitate size. The θ-Al_2O_3 peaks were much weaker in the FS sample than in the MS and CS samples.

Figure 6 shows the cross-sectional STEM microstructures of the samples after oxidation for 10 min. The supersaturated single-γ sample formed a thin and homogeneous oxide scale with a duplex-layer structure. The EDS elemental maps shown in Fig. 7 indicate that the outer layer was Fe-containing Cr_2O_3 and the inner layer was α-Al_2O_3. The formation of α-Al_2O_3 in the inner layer was confirmed by the diffraction pattern shown in the inset of Fig. 6b. The FS sample also formed a thin and relatively homogeneous oxide scale. In addition to a duplex oxide scale similar to that formed on the supersaturated single-γ sample, a single oxide layer slightly thicker than the duplex scale was observed, as shown in Fig. 6e. Although the diffraction pattern obtained from this layer was nearly ring-like owing to its fine grain structure, this oxide scale was most likely θ-Al_2O_3 based on the XRD profile shown in Fig. 5b. A thick oxide scale accompanied by internal oxide precipitates also formed locally on the γ matrix region in the FS sample. In the MS and CS samples, three distinct types of oxide scales were observed. The thickest oxide scale consisted of an outer Fe- and Ni- containing Cr_2O_3 layer, and a region containing internal Al_2O_3 precipitates formed on the γ matrix region, as shown in Fig. 7d. A θ-Al_2O_3 layer was consistently observed just above the β precipitates, as shown in Figs. 6f, g, and 7c. In addition, a thinner duplex oxide scale, composed of an outer Cr_2O_3 and an inner α-Al_2O_3 layer, developed above the β/γ interfaces. These results indicate that the supply of solute element to the surface in the initial oxidation stage was inhomogeneous in the MS and CS samples, depending on the original alloy microstructure. In contrast, relatively homogeneous solute element supply occurred in the FS and supersaturated single-γ samples.

3.4 Oxidation for up to 1 h

Figure 8 shows the surface morphologies of the samples after oxidation for 1 h. A continuous and thin oxide scale with some blade-like oxides formed on the supersaturated single-γ sample. The EDS elemental maps shown in Fig. 8b suggest that these blade-like oxides were Al-rich. A similar surface morphology was observed on the FS sample. Blade-like Al-rich oxides formed in a network-like manner over most of the surface. Some thick Cr_2O_3-rich oxide grains, shown in Fig. 8d, formed locally. Smooth and relatively thin oxide regions were also observed within the network of Al-rich oxide ridges. In the MS

and CS samples, inhomogeneous oxide scales were observed, characterized by the coexistence of two types of oxide regions, dense and smooth Cr-rich oxides and blade-like Al-rich oxides.

Figure 9 shows the cross-sectional microstructures and elemental line profiles measured from the surface to the substrate after oxidation for 1 h. A homogeneous and thin oxide scale consisting of a single Al_2O_3-rich layer formed on the supersaturated single-γ sample. β precipitates were observed in the single-γ sample after the 1 h oxidation test. The FS sample also formed a continuous Al_2O_3 scale. However, oxide nodules were observed on the surface of the FS sample. A β-precipitate-free zone developed beneath the oxide layer in both the supersaturated single-γ and FS samples, and its thickness was smaller in the supersaturated single-γ sample than in the FS sample. The MS and CS samples formed inhomogeneous oxide scales consisting of thin oxide regions, similar to those observed in the FS sample, and thick oxide regions. The area fraction of the thin oxide scale tended to be larger in the MS sample than in the CS sample. The thick oxide scale formed on the MS and CS samples consisted of an outer Cr-rich oxide layer and an inner Al_2O_3 layer. Internal Al_2O_3 precipitates connected to the outer Cr-rich oxide layer were observed in the CS sample. In the CS sample, regions where Al_2O_3 formed were often located above β precipitates, as shown in Fig. 9f. In such regions, a thin β-precipitate-free zone, where β precipitates decomposed to supply Al to the matrix, was observed. The EPMA elemental profiles obtained along the dotted lines in the cross-sectional images confirmed the oxide scale structures and the formation of the β-precipitate-free zone beneath the oxide scale. The homogeneous thin oxide scale consisted of relatively pure Al_2O_3, whereas the thick duplex oxide consisted of a Cr-rich outer oxide layer and an internal Al_2O_3 layer.

4. Discussion

Although the alloy used in this study contains Fe, the oxide map of the Ni-Al-Cr system shown in Fig. 2 suggests that the nominal alloy composition, Ni-15Fe-20Cr-12Al-0.03Zr is located in the region where an external Al_2O_3 scale is expected to form. Consistent with this prediction, the supersaturated single γ sample formed a continuous α-Al_2O_3 scale during the initial oxidation stage and a similar oxide scale was formed on the FS sample. In contrast, the MS and CS samples formed inhomogeneous oxide scales consisting of thick Cr-rich oxide regions accompanied by internal Al_2O_3 precipitates and relatively thin Al_2O_3-rich regions. These results indicate that the local oxide scale structure is governed not simply by the average alloy composition but by the spatial distribution of Al and Cr associated with the γ-β two phase microstructure.

In addition, two polymorphs of Al_2O_3, θ- and α-Al_2O_3 were observed after oxidation for 10 min. Based on the analysis of the oxide scale formed on the supersaturated single γ sample, it can be regarded that the α-Al_2O_3 scale was always observed beneath a Cr_2O_3 layer as part of a duplex oxide scale, whereas θ-Al_2O_3 was always observed as a single oxide layer above β precipitates. It is well known that metastable Al_2O_3 scales can form during the initial oxidation of Ni-Al alloys at around 1000°C and subsequently transform into stable α-Al_2O_3 scale. This transformation behavior has been widely investigated for Al_2O_3-

forming alloys, and the transformation has been reported to require a long time in β-(Ni, Fe)Al [26]. In contrast, Fe and Cr addition are known to accelerate the transformation to α-Al_2O_3 because Fe_2O_3 and Cr_2O_3 can act as structural templates for α-Al_2O_3 formation [27–30]. In the present study, Cr was partitioned preferentially into the γ phase, whereas Al was enriched in the β phase.

Figure 10 schematically summarizes the initial oxidation process in the samples with different initial microstructures. In the supersaturated single-γ sample, Cr and Al are supplied relatively homogeneously and sufficiently to the surface. Therefore, a thin and continuous duplex oxide scale, consisting of an outer Cr_2O_3 and an inner α-Al_2O_3 layers, forms during the initial oxidation stage, as shown in Fig. 10a, d, **and g**. In the very early oxidation stage, a thin Cr_2O_3 scale is considered to form initially, followed by the formation of α-Al_2O_3 beneath it [31]. For the samples containing β-precipitates, the β/γ interface plays a particularly important role in the initial oxidation stage because it is the region where Cr can be supplied from the γ matrix and Al can be supplied from the β precipitates. In the FS sample, the high γ/β interface density enhances the Al supply through rapid dissolution of fine β precipitates. At the same time, the short diffusion distances and high interface density make the solute supply more homogeneous than in the MS and CS samples. As a result, sufficient Al and Cr can be supplied to the surface, allowing the formation of a relatively continuous and thin Al_2O_3 scale even above regions originally corresponding to the γ-matrix [7]. However, because the solute distribution is still less homogeneous than that in the supersaturated single-γ sample, the oxide scale formed on the FS sample is slightly less uniform, as illustrated in Figs. 10e and 4f.

In the MS and CS samples, the γ matrix regions are relatively large, and the Al supply is insufficient to form a continuous external Al_2O_3 layer over the entire γ matrix surface during the initial oxidation stage. As a result, a relatively thick Cr_2O_3 layer accompanied by internal Al_2O_3 precipitates forms above the γ matrix regions. In contrast, around the β precipitates, Al can be supplied from the β phase, while Cr can be supplied from the surrounding γ matrix. This combined supply promotes the initial formation of a Cr_2O_3 scale and accelerates the transformation from θ-Al_2O_3 to α-Al_2O_3 near the β/γ interface. Consequently, a thin duplex oxide scale with an outer Cr_2O_3 and an inner α-Al_2O_3 layers forms in the narrow regions surrounding the β-precipitates, as shown schematically in Fig. 10f and **i**. Above the β precipitates, the high Al content allows the formation of an Al_2O_3 layer; however, because the Cr supply from the β precipitates is limited, the transformation of from θ-Al_2O_3 to α-Al_2O_3 is delayed [26, 32, 33]. Therefore, a single θ-Al_2O_3 scale remains above the β precipitates for a longer time. Since θ-Al_2O_3 scale generally grows faster than α-Al_2O_3 scale, the regions covered by θ-Al_2O_3 become thicker than those covered by the duplex Cr_2O_3/α-Al_2O_3 scale.

After prolonged oxidation, internal Al_2O_3 precipitates formed beneath the Cr-rich oxide in the γ matrix regions gradually develop into a continuous α-Al_2O_3 layer in the MS and CS samples. Once this continuous Al_2O_3 layer is established, the further growth rate of oxide scale decreases. This explains why the difference in the oxidation kinetics is pronounced mainly during the initial oxidation stage,

whereas the oxidation rates of all samples become similarly low after longer oxidation times, as shown in Fig. 3.

5. conclusion

In this study, the effect of microstructure, particularly β precipitate size, on the high temperature oxidation behavior of a Ni-12Al-20Cr-15Fe-0.03Zr alloy was systematically investigated. The main conclusions are summarized as follows.

1. The formation of β precipitates increased the initial mass gain compared with the supersaturated single γ sample. Among the γ-β two phase samples, the mass gain increased with increasing β precipitate size, indicating that coarse β precipitates are detrimental to the initial oxidation resistance.
2. The supersaturated single-γ sample formed a thin and continuous duplex oxide scale consisting of an outer Cr_2O_3 and an inner α-Al_2O_3 layers. This scale formation was attributed to the homogeneous and sufficient supply of both Al and Cr from the supersaturated γ substrate.
3. The local oxide scale structure in the γ-β phase samples depended strongly on the underlying microstructure. Above β precipitate, a single θ-Al_2O_3 scale formed because of the high Al supply and limited Cr supply. In contrast, near the β/γ interfaces, a duplex Cr_2O_3/α-Al_2O_3 scale formed because Al was supplied from the β precipitates and Cr was supplied from the γ matrix.
4. In the γ-matrix regions away from β precipitates, especially in the MS and CS samples, a thick Cr_2O_3 scale accompanied by internal Al_2O_3 precipitates formed because the Al supply from the γ-matrix was insufficient to establish a continuous external Al_2O_3 scale during the initial oxidation stage.
5. These results indicate that β precipitate size is a critical microstructural parameter governing the initial high temperature oxidation behavior. Fine β precipitates, with a higher β/γ interface density, promote more homogeneous Al supply and facilitate the formation of a protective Al_2O_3 scale, whereas coarser β precipitates result in more inhomogeneous oxide scale formation.

Declarations

Declaration of Competing Interest

The authors declare that they have no known competing financial interests or personal relationships that could have appeared to influence the work reported in this paper.

Author Contribution

Zhentao Wang wrote the main manuscript text and prepared figures 1-10. All authors reviewed the manuscript.

Acknowledgements

This research received no specific grant from any funding agency.

Data availability

Data will be made available on request.

References

1. G. K. Salwan, R. Subbarao, S. Mondal. *Materials Today: Proceedings* 46, 2021 (8864–8870).
2. F. Findik. *Heritage and Sustainable Development* 5.2, 2023 (213).
3. A. N. Singh, S. K. Swain, A. Meena, M. Islam, K. Nam. *Ceramics* 7.4, 2024 (1928–1963).
4. A. Familifard, A. A. Amadeh, S. Raygan, R. Gholamipour. *Journal of Materials Research* 38.5, 2023 (1197–1210).
5. V. B. Trindade, U. Krupp, P. Wagenhuber, H. Christ. *Materials and Corrosion* 56.11, 2005 (785–790).
6. V. Trindade, H. Christ, U. Krupp. *Oxidation of metals* 73.5, 2010 (551–563).
7. Z. Wang, S. Hayashi, S. Yoneda, A. Shaaban, M. Ueda. *High Temperature Corrosion of Materials* 103.4, 2026 (66).
8. K. Bochenek, M. Basista. *Progress in Aerospace Sciences* 79, 2015 (136–146).
9. E. P. Busso, F. A. McClintock. *Acta metallurgica et materialia* 42.10, 1994 (3263–3275).
10. H. Pei, Z. Wen, Y. Zhang, Z. Yue. *Applied Surface Science* 411, 2017 (124–135).
11. X. Zhuang, Y. Tan, X. You, P. Li, L. Zhao, C. Cui, H. Zhang, H. Cui. *Vacuum* 189, 2021 (110219).
12. D. Li, J. Chen, I. P. Etim, Y. Liu, C. Wu, J. Wang, X. Su. *Vacuum* 194, 2021 (110582).
13. S. Zhou, M. Hu, C. Li, Q. Guo, L. Yu, H. Ding, Y. Liu. *Materials Science and Engineering: A* 855, 2022 (143954).
14. L. Zhou, A. Mehta, K. Cho, Y. Sohn. *Journal of Alloys and Compounds* 727, 2017 (153–162).
15. J. Engkvist, U. Bexell, M. Grehk, M. Olsson. *Materials and corrosion* 60.11, 2009 (876–881).
16. R. Darolia, D. F. Lahrman, R. D. Field, J. R. Dobbs, K. M. Chang, E. H. Goldman, D. G. Konitzer. *Ordered Intermetallics—Physical Metallurgy and Mechanical Behaviour* Dordrecht: Springer Netherlands, 1992 (679–698).
17. Y. Zhai, Y. Chen, Y. Zhao, H. Long, X. Li, Q. Deng, H. Lu, X. Yang, G. Yang, W. Li, L. Yang, S. Mao, Z. Zhang, A. Li, X. Han. *Acta Materialia* 215, 2021 (116991).
18. Yurek, J. Gregory. *Corrosion Mechanisms*, 2020 (397–446).
19. Q. Lu, J. Wang, H. Li, S. Jin, G. Sha, J. Lu, L. Wang, B. Jin, X. Lan, L. Li, K. Li, Y. Du. *Nature Communications* 14.1, 2023 (2959).

20. E. Wessel, V. Kochubey, D. Naumenko, L. Niewolak, L. Singheiser, W. J. Quadakkers. *Scripta Materialia* 51.10, 2004 (987–992).
21. S. Hayashi, H. Utsumi, S. Omori, S. Yoneda. *Corrosion Science* 209, 2022 (110751).
22. S. Hayashi, T. Narita, B. Gleeson. *Materials science* 522, 2006 (229–238).
23. J. L. Smialek, N. S. Jacobson. *High temperature materials and mechanisms*, 2014 (95–162).
24. G. R. Wallwork, A. Z. Hed. *Oxidation of Metals* 3.2, 1971 (171–184).
25. J. D. Osorio, A. Toro, J. P. Hernandez-Ortiz. *Dyna* 79.176, 2012 (149–158).
26. S. Hayashi, Y. Takada, S. Yoneda, S. Ukai. *Oxidation of Metals* 86.1, 2016 (151–164).
27. Y. Huang, X. Peng. *Corrosion Science* 112, 2016 (226–232).
28. Y. Suzue, S. Hayashi, S. Ukai. *Oxidation of Metals* 89.1, 2018 (81–97).
29. A. Khan, Y. Huang, Z. Dong, X. Peng. *Corrosion Science* 150, 2019 (91–99).
30. M. W. Brumm, H. J. Grabke. *Corrosion science* 33.11, 1992 (1677–1690).
31. S. Yoneda, S. Hayashi, S. Ukai. *Oxidation of Metals* 89.1, 2018 (81–97).
32. Z. Liu, W. Gao. *Oxidation of Metals* 54.3, 2000 (189–209).
33. Y. Kitajima, S. Hayashi, T. Nishimoto, T. Narita, S. Ukai. *Oxidation of Metals* 73.3, 2010 (375–388).

Figures

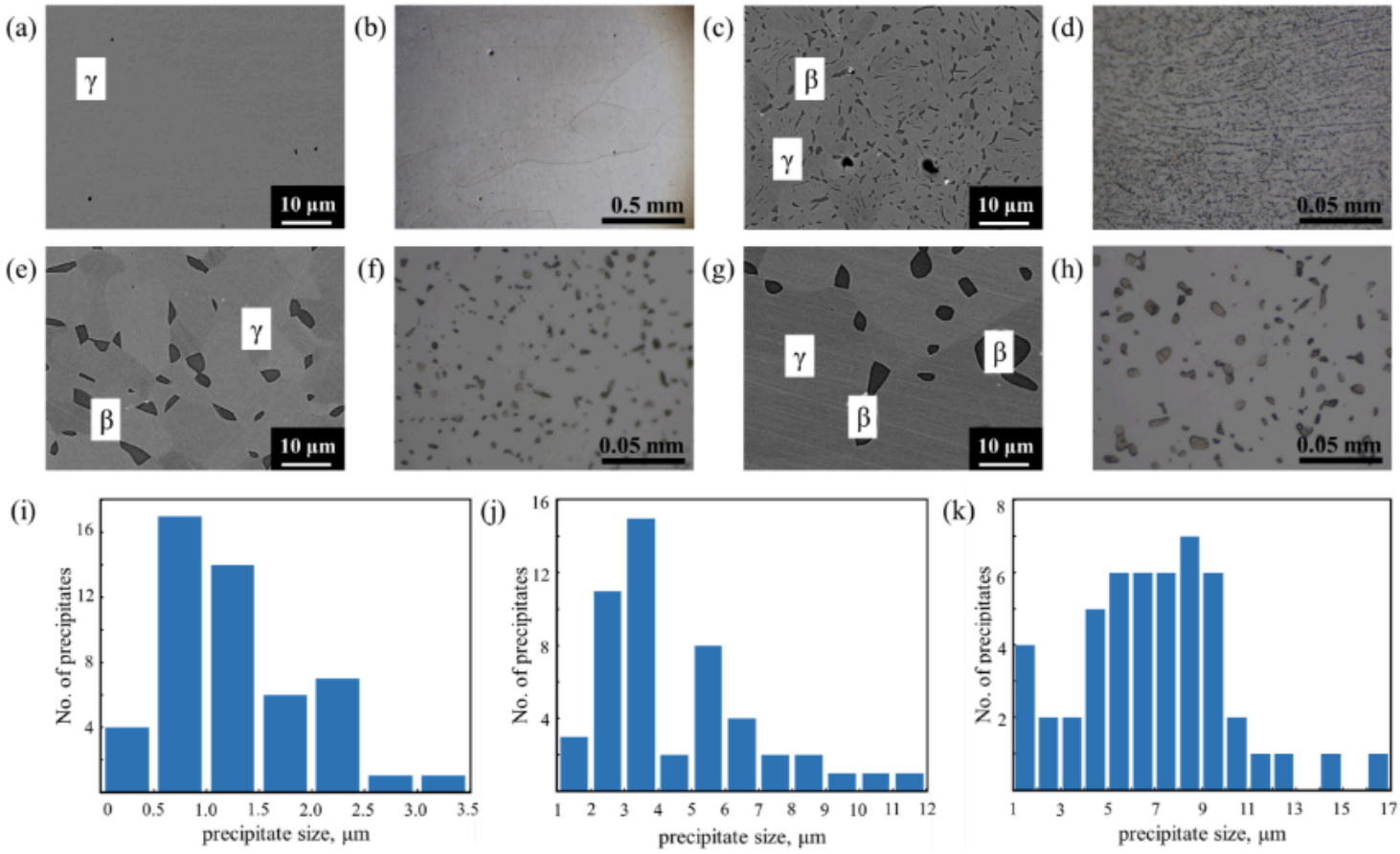


Figure 1

Microstructures of (a, b) supersaturated single-γ phase sample, (c, d) the FS, (e, f) the MS, (g, h) the CS samples, and the statistical data on the size of 50 precipitates in (i) the FS, (j) the MS, and (k) the CS samples. Panels (b, d, f, h) show optical microscopy images of the etched samples.

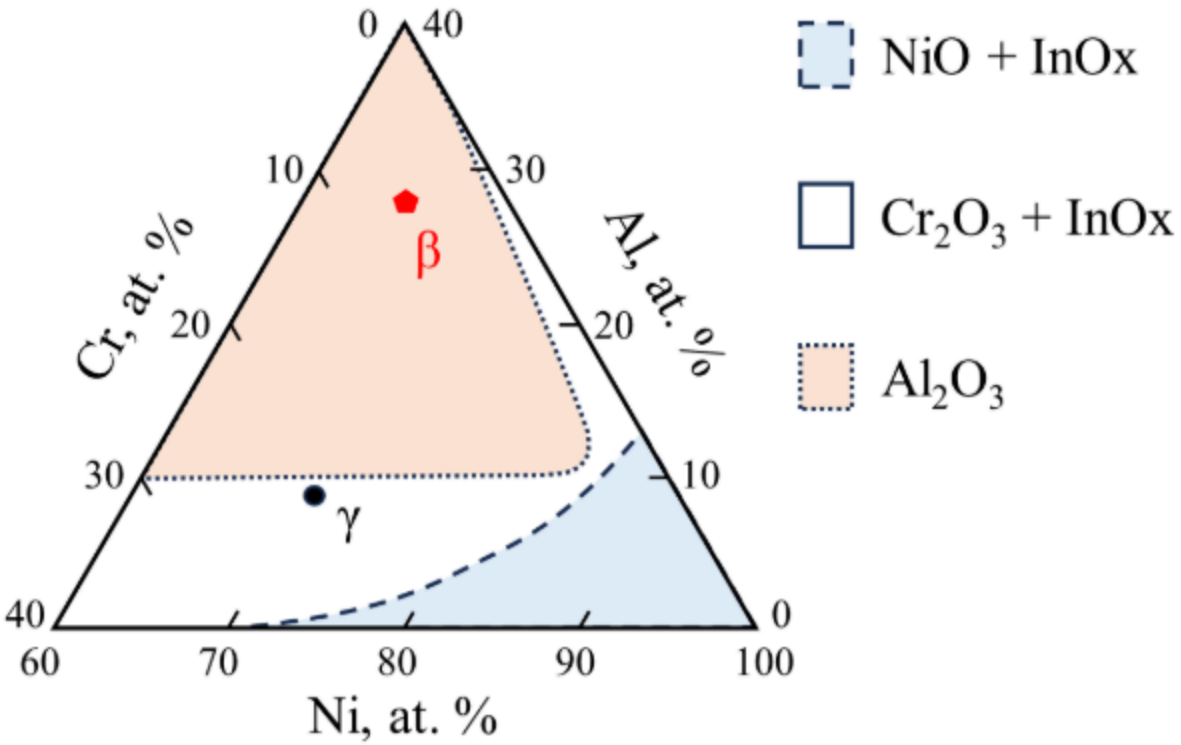


Figure 2

The oxide map of Ni-Al-Cr [25] system at 1000 °C. The red pentagonal and black circular marks indicate the composition of the β phase and γ phase, respectively.

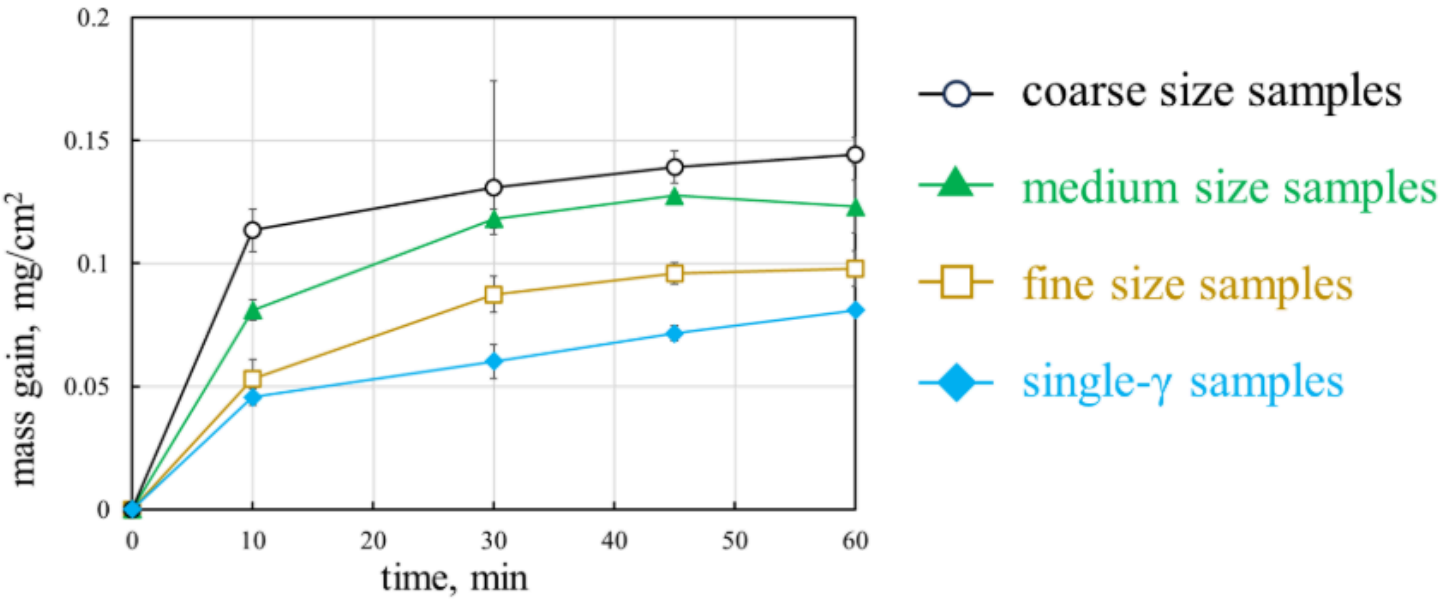


Figure 3

the oxidation kinetics of samples oxidized at 1000 °C in air for up to 60 min.

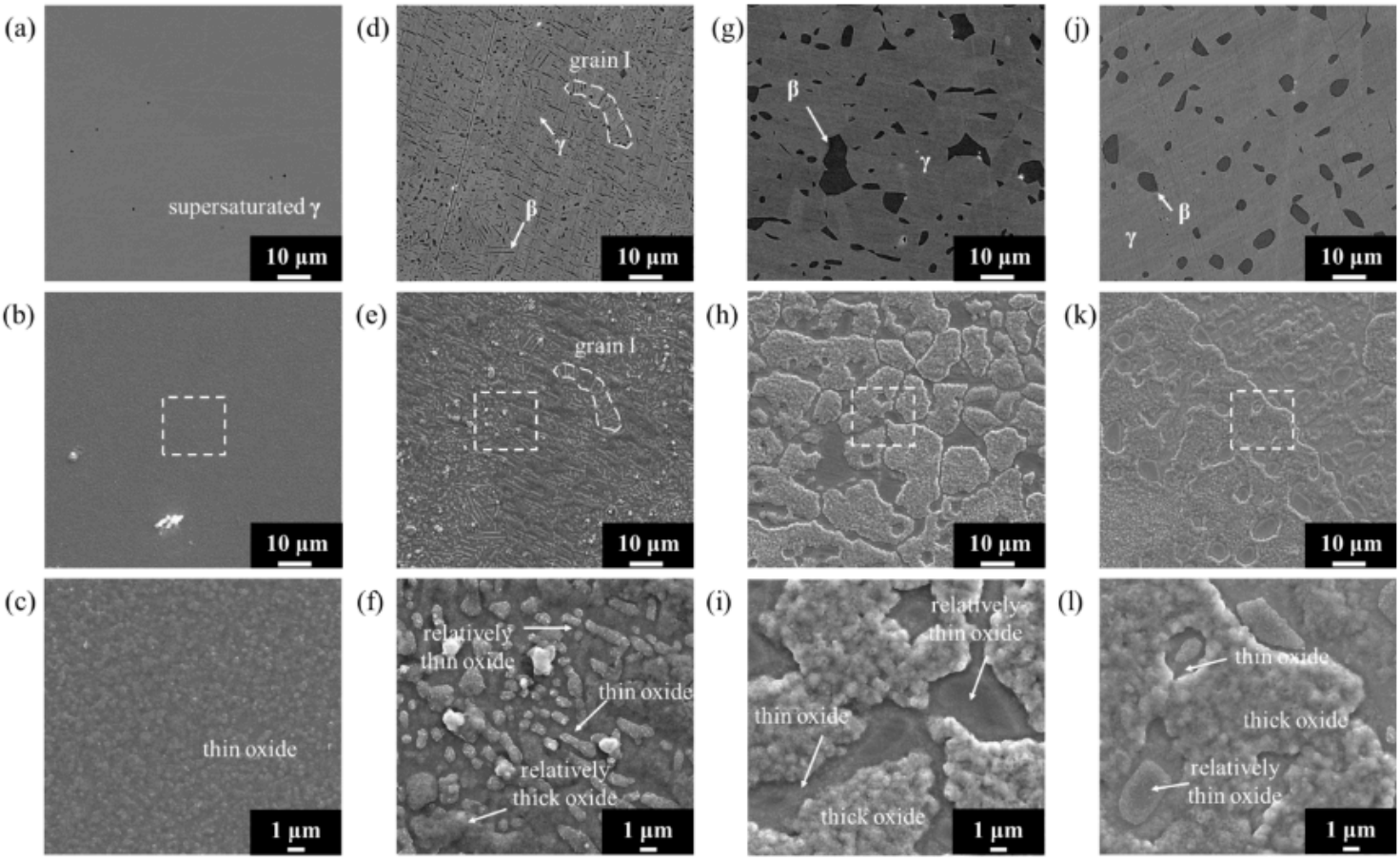


Figure 4

Surface morphologies of samples before and after oxidation for 10 min. (a-c) supersaturated single-γ phase sample, (d-f) FS sample, (g-i) MS sample, and (j-l) CS sample. Panels (c, f, i, and l) show enlarged images of the regions indicated by dotted rectangles.

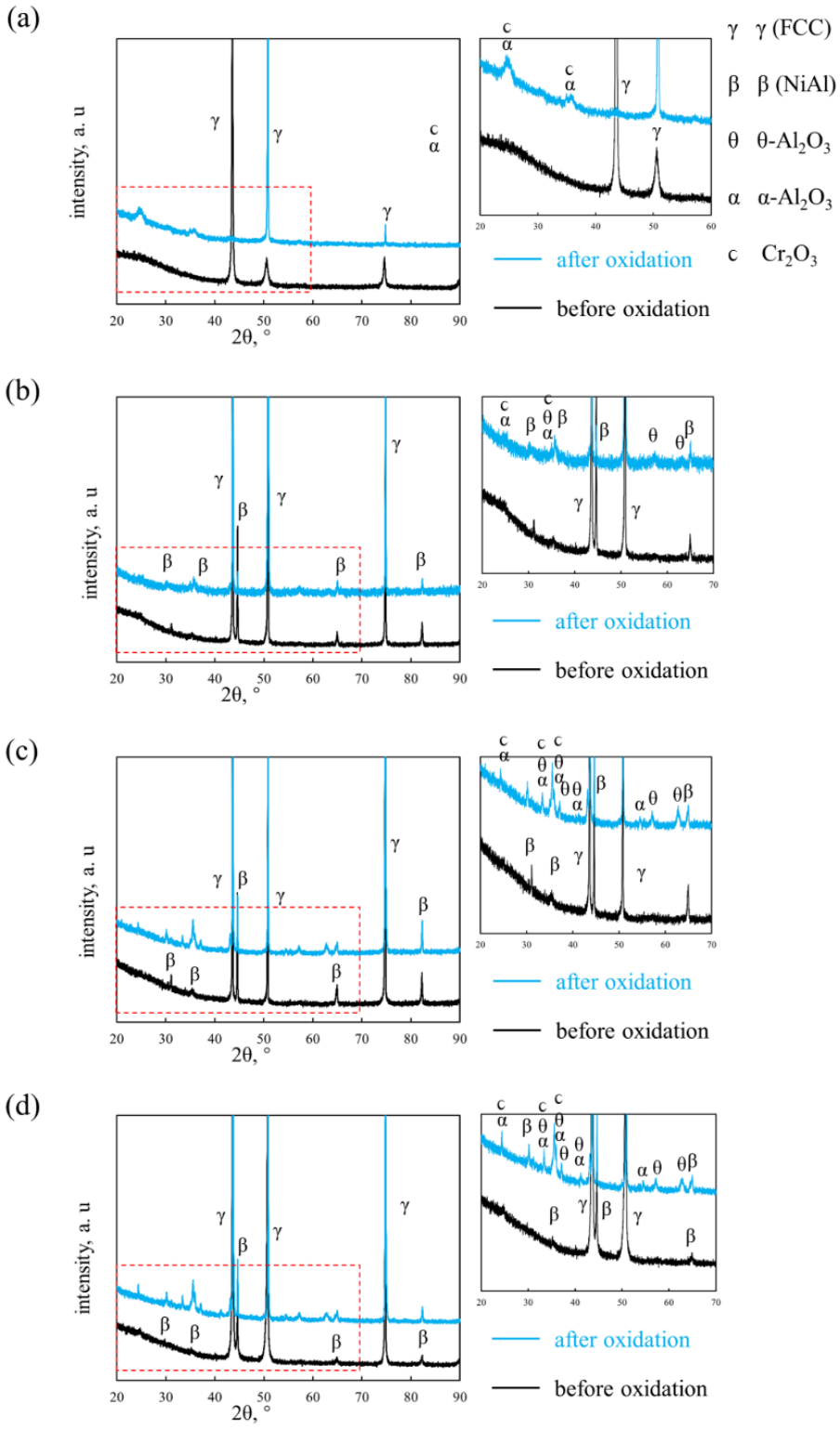


Figure 5

XRD profiles and enlarged views of the profiles before and after oxidation for 10 min. (a) supersaturated single-γ phase sample, (b) FS sample, (c) MS sample and (d) CS sample

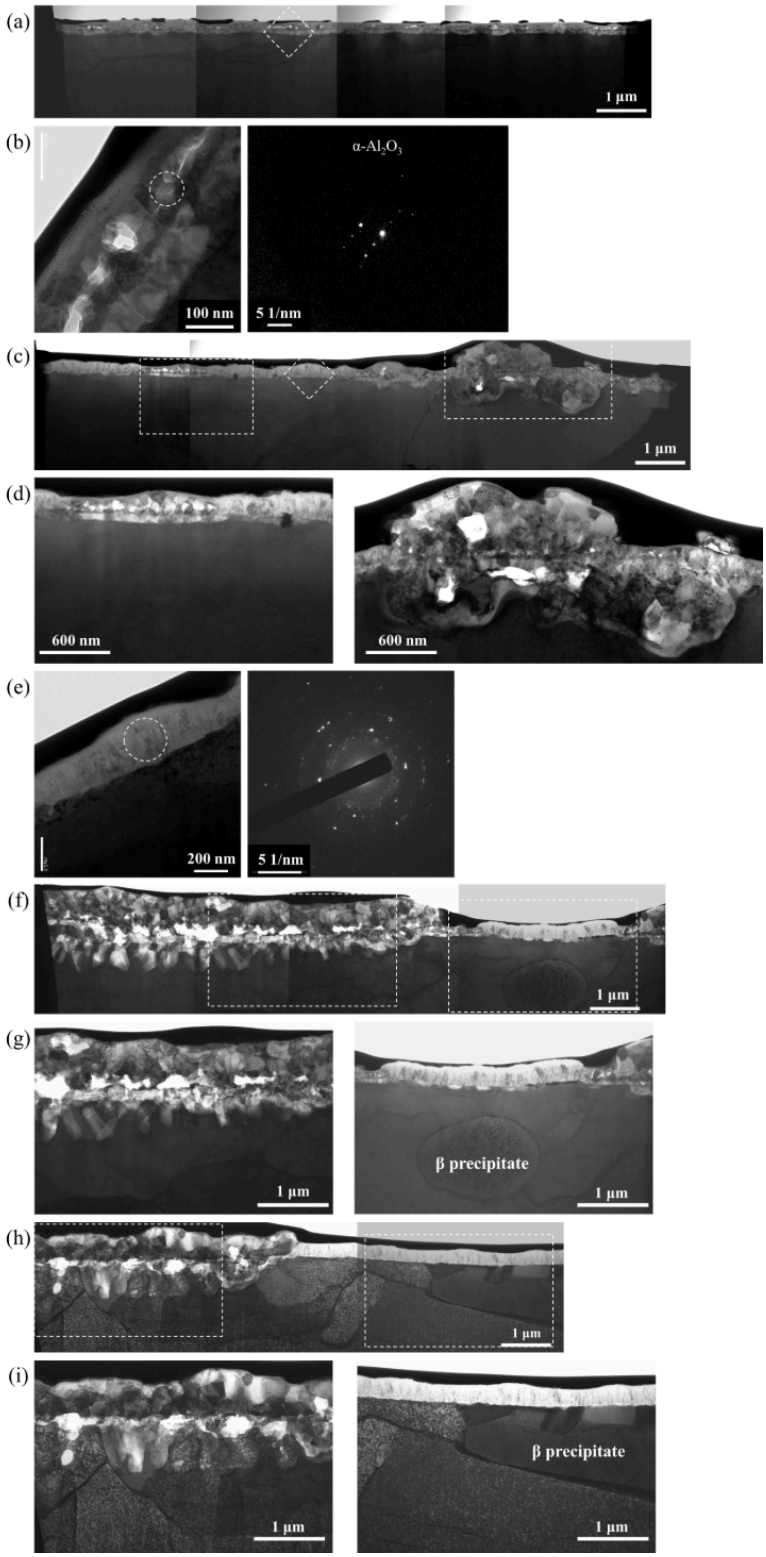


Figure 6

Cross-sectional STEM microstructures of samples after oxidation for 10 min. (a, b) supersaturated single-γ sample, (c, d, and e) FS sample, (f, g) MS sample, and (h, i) CS sample. Panels (b, d, g, and i)

show enlarged images of the regions indicated in (a, c, f, h), respectively. The insets in (b) and (e) show diffraction patterns obtained from the regions indicated by dotted areas in (a) and (c), respectively.

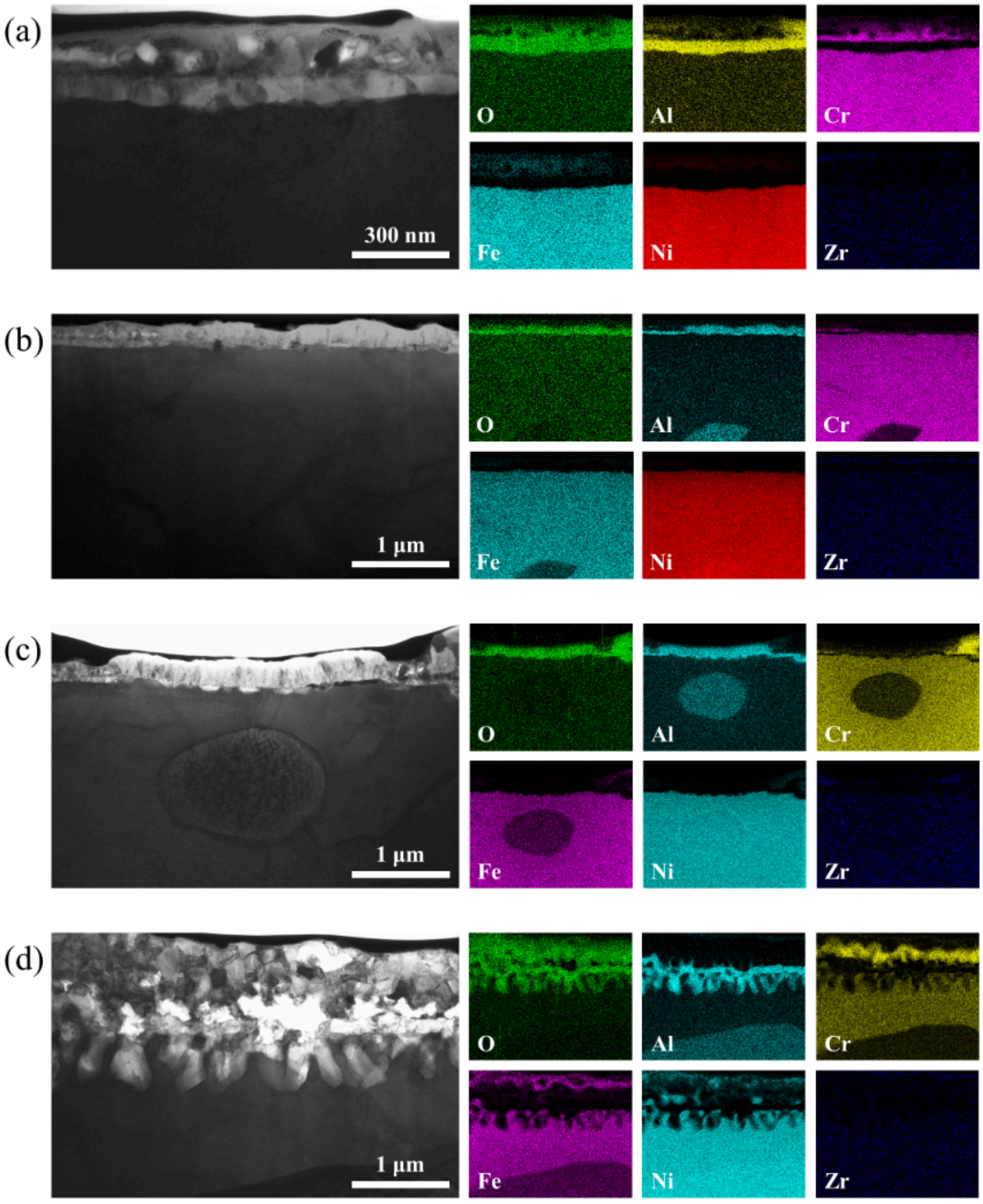


Figure 7

EDS elemental maps of the oxide scales formed after oxidation for 10 min. (a) duplex oxide scale formed on the supersaturated single-γ sample, (b) single-layer oxide scale formed on the FS sample, (c)

thin oxide scale formed above β precipitates in the MS sample, and (d) thick oxide scale formed above the γ-matrix in the CS sample.

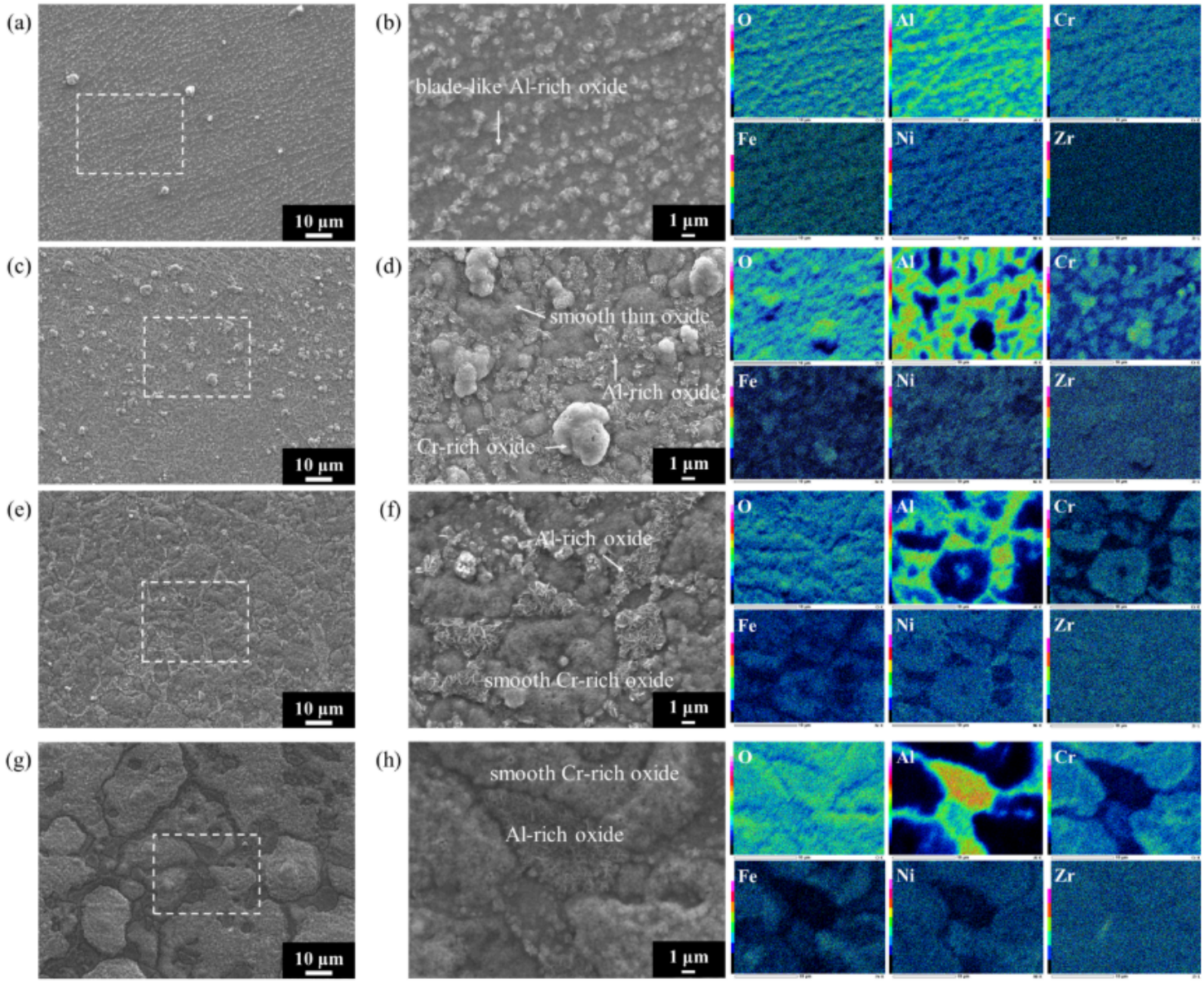


Figure 8

Surface morphologies of the samples after oxidation for 1 h. (a, b) supersaturated single-γ phase sample, (c, d) FS sample, (e, f) MS sample, and (g, h) CS sample. Panels (b, d, f, and h) show enlarged images of the dotted areas and the corresponding elemental maps.

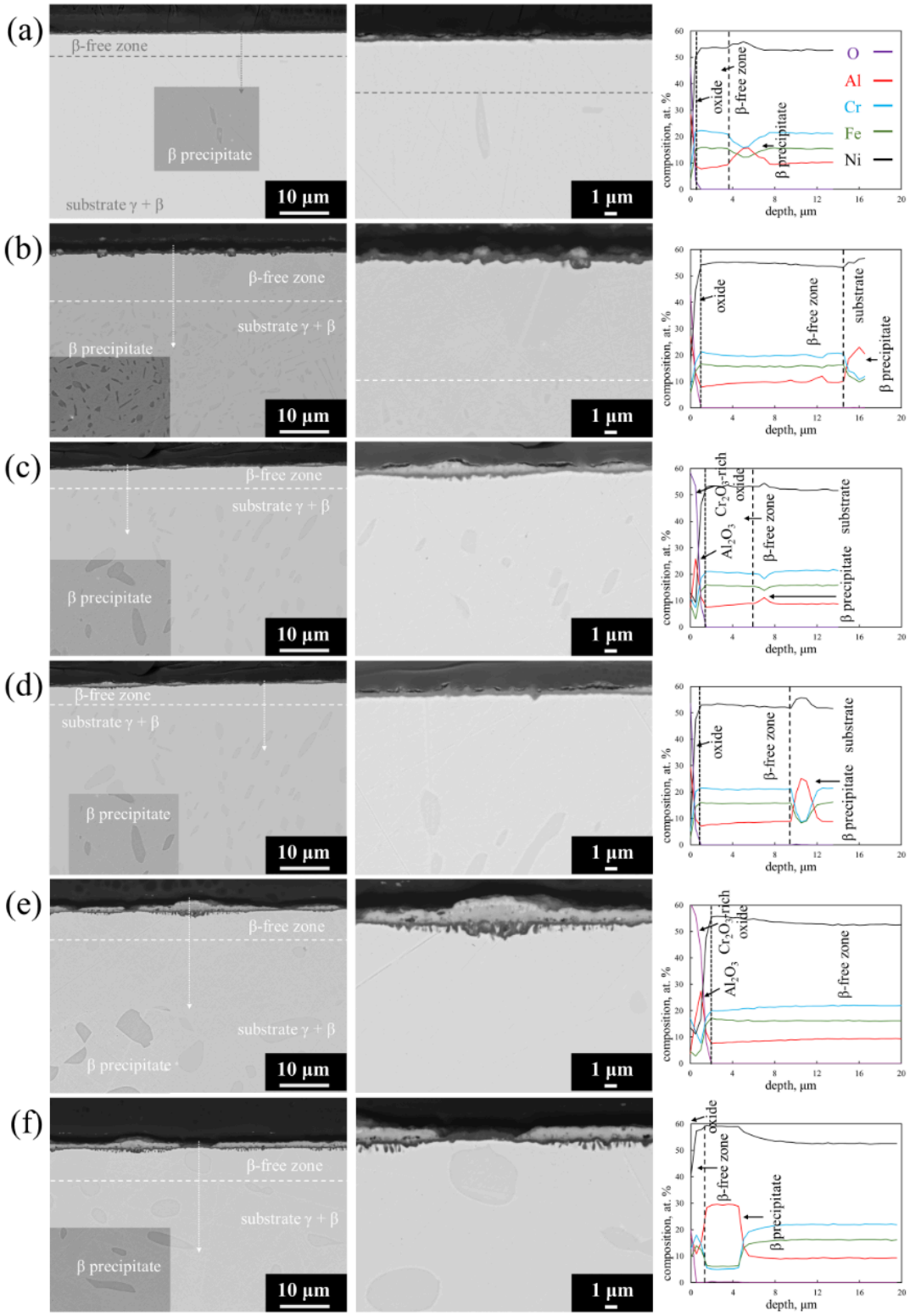


Figure 9

the cross-sectional microstructures, enlarged images of oxide scale, and elemental profiles of the samples after oxidation for 1 h. (a) supersaturated single-γ sample, (b) FS sample, (c, d) MS sample, and (e, f) CS sample.

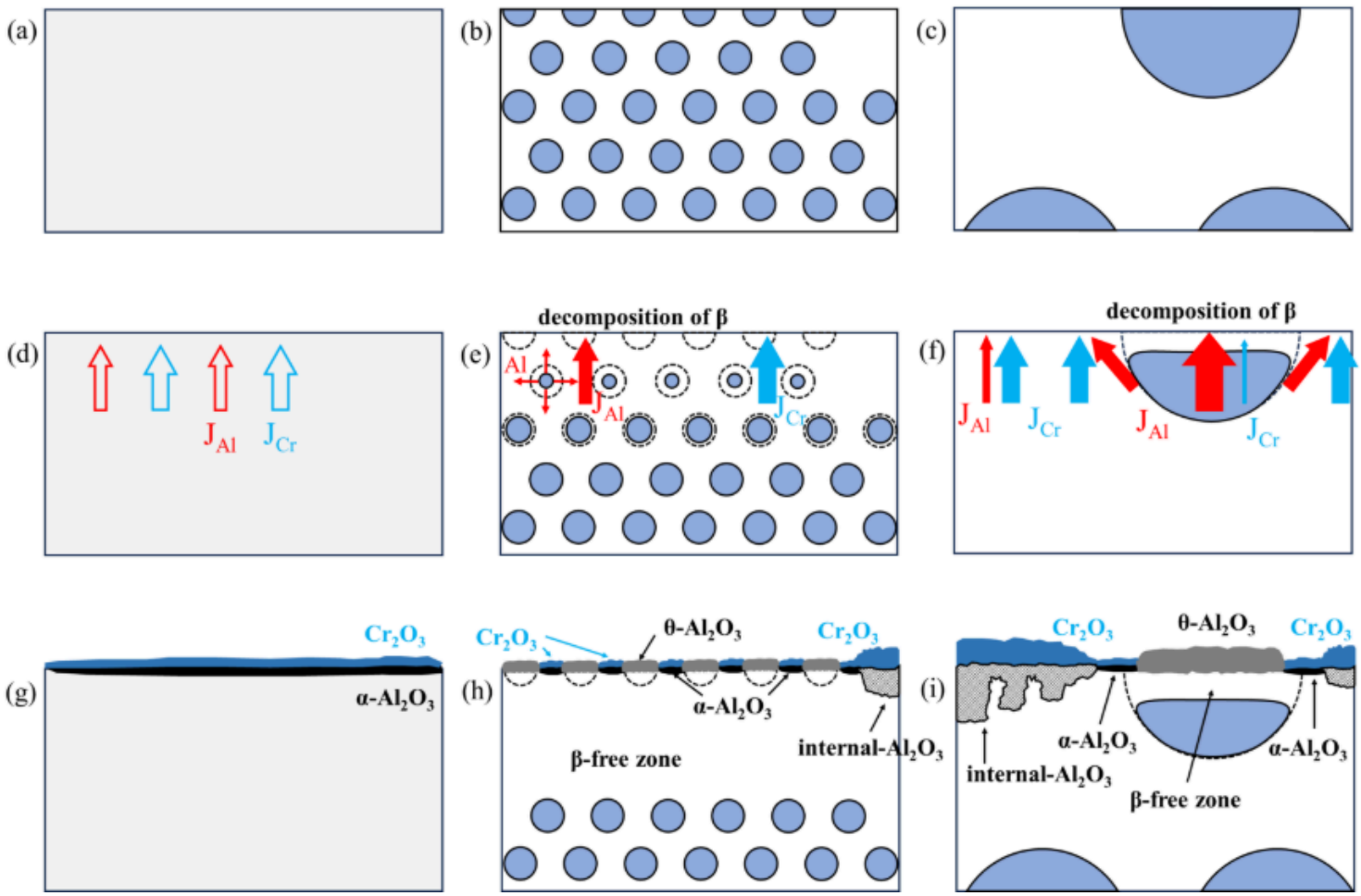


Figure 10

Schematic models of the initial oxidation process in samples with different initial microstructure. (a, d, g) supersaturated single-γ sample, (b, e, h) FS sample, and (c, f, i) CS sample. Panels (a-c) illustrate the original structure of samples, panels (d-f) illustrate the local Al and Cr supply due to decomposition of β precipitates, and panels (g-i) illustrate the resulting oxide scale structure.